

Response of active Brownian particles to boundary drivingCaleb G. Wagner^{✉,*}, Michael F. Hagan[†] and Aparna Baskaran[‡]*Martin Fisher School of Physics, Brandeis University, Waltham, Massachusetts, USA*

(Received 31 May 2019; revised manuscript received 21 August 2019; published 18 October 2019)

We computationally study the behavior of underdamped active Brownian particles in a sheared channel geometry. Due to their underdamped dynamics, the particles carry momentum a characteristic distance away from the boundary before it is dissipated into the substrate. We correlate this distance with the persistence of particle trajectories, determined jointly by their friction and self-propulsion. Within this characteristic length, we observe counterintuitive phenomena stemming from the interplay of activity, interparticle interactions, and the boundary driving. Depending on the values of friction and self-propulsion, interparticle interactions can either aid or hinder momentum transport. More dramatically, in certain cases we observe a flow reversal near the wall, which we correlate with an induced polarization of the particle self-propulsion directions. We rationalize these results in terms of a simple kinetic picture of particle trajectories.

DOI: [10.1103/PhysRevE.100.042610](https://doi.org/10.1103/PhysRevE.100.042610)**I. INTRODUCTION**

Systems which are driven far from equilibrium exhibit emergent phenomena that are strikingly different from the thermodynamically allowed behaviors of equilibrium systems. Recently, intense research has focused on a class of such systems known as active matter, in which driving enters the system at the level of its microscopic constituents [1–10]. Active matter occurs on many scales, from the microscopic and colloidal to the macroscopic. Specific examples include the cell cytoskeleton [11], reconstituted biopolymers and molecular motors [11,12], bacterial suspensions [13,14], synthetic self-propelled colloids [15–20], schooling fish [21,22], and flocking birds [23].

Progress toward a fundamental understanding of active matter requires minimal models that are sufficiently tractable to describe theoretically but exhibit the key phenomenology of more complicated, real-world systems. Toward this end, a common paradigm is to consider particles which self-propel as a result of an internal driving force acting along some body axis. For example, the active Brownian particle (ABP) model describes spheres or disks that self-propel at constant velocity and whose direction of propulsion evolves diffusively [24]. Despite their simplicity, such self-propelled particle models exhibit striking emergent phenomena, including athermal phase separation [25–36], spontaneous flows [37–42], and long-range density variations [43–47]. However, researchers have only recently begun to study these models in the presence of *external* driving. Previous work has examined the response of self-propelled particles to perturbing external fields [48] and time-periodic compression and expansion [49]. Efforts have also been made to construct a formal theoretical framework of response and transport in active materials, using an

Irving-Kirkwood-type approach [50,51], a multiple-timescale analysis [52], or large deviation theory [53].

It has been established that boundaries have dramatic and long-ranged effects in active systems, which make active systems nonextensive (i.e., their behaviors are not independent of system size) [44,46,47,54–57]. However, the consequences of boundary *driving* have yet to be addressed in the literature of active particles. In this article, we begin to address this question by performing computer simulations of an underdamped ABP system subject to shearing forces applied at the boundary. We characterize the response of the system in terms of the flow velocity profile—defined as the average particle velocity at a given position—and analyze the results in the context of a simple kinetic picture of particle trajectories.

In general, the flow velocity profile decays exponentially with distance from the boundary. We denote the length of this decay as the *penetration depth*, which generically depends on the friction and self-propulsion forces. Interestingly, we find that interparticle interactions can either aid or hinder momentum transport depending on the system parameters. This stands in contrast with systems of passive spheres, where interactions generically enhance momentum transport.

To shed light on possible boundary conditions applicable to continuum theories of rheology of active fluids, we consider also the properties of the system *at* the wall, i.e., on the order of a particle diameter from the wall. In further contrast to equilibrium systems, we discover a flow reversal phenomenon within this region, where the flow velocity points opposite to the boundary driving. Finally, we find that the stress at the wall is a nontrivial function of the density of the system.

We rationalize these findings in terms of a simple kinetic picture of how ABPs move and interact in the presence of shear stress. We conclude that the response of ABPs to boundary driving is dominated by a boundary layer on the scale of the persistence of particle trajectories. Finally, we discuss the implications of our results for developing a more systematic theoretical description of response and transport in systems of self-propelled particles.

*kswag@brandeis.edu

†hagan@brandeis.edu

‡aparna@brandeis.edu

II. MODEL AND SIMULATIONS

A. Equations of motion

We work within the active Brownian particle (ABP) model, which is an idealized model system that captures important features of several experimental active matter systems, such as vibration-fluidized granular matter and chemically propelled colloidal particles [15,20,29,58]. In general, ABPs are self-propelled spheres with diffusive reorientation statistics. In our case we specialize to two-dimensional systems in which the translational center-of-mass dynamics is underdamped with corresponding friction coefficient ξ . Physically, this can be conceptualized as particle motion on a two-dimensional dissipative substrate. Although many previous investigations of ABPs have assumed the overdamped limit, we require the more general underdamped dynamics to study momentum transport. Note also that underdamped dynamics is required to accurately describe some features of other active systems [59–61]. On the other hand, we keep the angular dynamics overdamped, since angular inertia is expected to play only a secondary role in the transport of linear momentum. The equations of motion are then

$$\frac{d\mathbf{r}}{dt} = \mathbf{v}, \quad (1)$$

$$\frac{d\mathbf{v}}{dt} = \frac{F_p}{m}\hat{\mathbf{u}} - \frac{1}{m}\nabla V_{\text{WCA}} - \xi\mathbf{v} + \sqrt{2D}\xi\eta^{\text{T}}(t), \quad (2)$$

$$\frac{d\theta}{dt} = \sqrt{2D_r}\eta^{\text{R}}(t). \quad (3)$$

Here $\eta^{\text{T}}(t)$ and $\eta^{\text{R}}(t)$ are δ -correlated thermal noises, satisfying $\langle \eta(t)\eta(t') \rangle = \delta(t-t')$ with corresponding diffusion coefficients D and $D_r = 3D/\sigma^2$. The self-propulsion enters as the constant magnitude force F_p in the direction of a particle's orientation $\hat{\mathbf{u}} = (\cos\theta, \sin\theta)$. In particular, the combination of self-propulsion and diffusive reorientation allows one to define an *active persistence length* $\ell = F_p/(m\xi D_r)$, which in the overdamped limit ($\xi \rightarrow \infty$ with $m\xi$ fixed) gives the distance over which a free particle's motion is correlated [24]. Interparticle interactions are described by a WCA potential [62]

$$V_{\text{WCA}}(r) = \begin{cases} 4\epsilon\left[\left(\frac{\sigma}{r}\right)^{12} - \left(\frac{\sigma}{r}\right)^6\right] + \epsilon & r \leq 2^{1/6}\sigma \\ 0 & r > 2^{1/6}\sigma \end{cases}. \quad (4)$$

In simulations we nondimensionalize using σ as the unit length and $\tau = \sigma^2/D$ as the unit time, and we set the WCA well-depth parameter equal to the thermal energy, $\epsilon = k_{\text{B}}T$. Denoting the new coordinates with primes, Eqs. (1)–(3) become

$$\frac{d\mathbf{r}'}{dt'} = \mathbf{v}', \quad (5)$$

$$\frac{d\mathbf{v}'}{dt'} = 3\xi_0\ell_0\hat{\mathbf{u}} - \xi_0\nabla V_{\text{WCA}} - \xi_0\mathbf{v}' + \sqrt{2}\xi_0\eta^{\text{T}}(t'), \quad (6)$$

$$\frac{d\theta}{dt'} = \sqrt{6}\eta^{\text{R}}(t'). \quad (7)$$

Thus the control parameters of a single-particle trajectory in free space are the nondimensional friction constant $\xi_0 = \xi\tau$ and active persistence length $\ell_0 = \ell/\sigma$. Note that due to

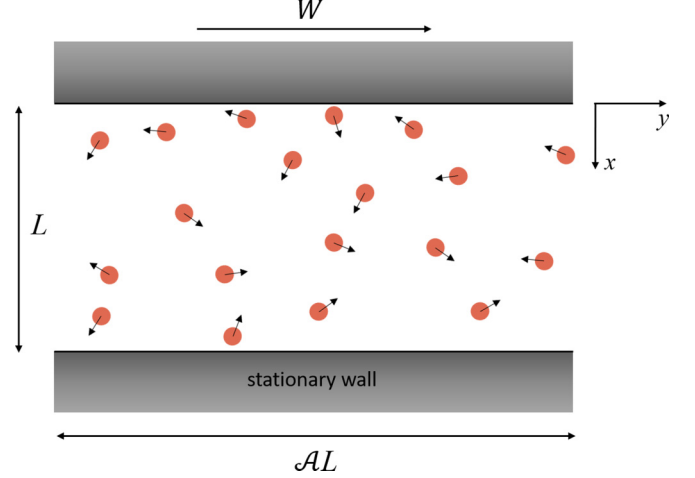


FIG. 1. The shearing geometry. The aspect ratio \mathcal{A} and packing fraction ϕ are varied to achieve a fixed overall number of particles.

the choice of units, $3\ell_0$ is the same as the Péclet number. In addition, the quantity $\xi/D_r = \xi_0/3$ expresses the relative magnitude of frictional versus rotational relaxation.

B. Shearing geometry

To understand the effects of boundary driving on this model, we consider a simple shearing geometry (Fig. 1), with periodic boundary conditions in the y direction and confining walls in the x direction. The bottom wall is stationary, and the upper wall moves with constant velocity W . In the y direction a force drives particles in contact with the wall in the direction of the wall's motion. We use a linear force, so the y component of the force at the upper wall is given by

$$F_{w,y}^{\text{upper}}(x, v_y) = \begin{cases} -b(v_y - W) & x \leq (2^{1/6} - 1)\sigma \\ 0 & x > (2^{1/6} - 1)\sigma \end{cases}, \quad (8)$$

for a particle with velocity v_y . Thus, the particles feel the wall potential within a distance from the wall $x \leq (2^{1/6} - 1)\sigma \simeq 0.12\sigma$. Unless noted otherwise, we take $b = 50(mD/\sigma^2)$ and $W = 5(D/\sigma)$. The x component of the wall force is just a short-range repulsion:

$$F_{w,x}^{\text{upper}}(x) = \begin{cases} V_{\text{WCA}}(x + \sigma) & x \leq (2^{1/6} - 1)\sigma \\ 0 & x > (2^{1/6} - 1)\sigma \end{cases}, \quad (9)$$

with V_{WCA} as defined in Eq. (4). This form of the wall force was chosen for simplicity; our results would not qualitatively change for other functional forms. Since the bottom wall is stationary and frictionless, it exerts a repulsive force in the x direction but no force in the y direction:

$$F_{w,x}^{\text{bottom}}(x) = \begin{cases} V_{\text{WCA}}(L - x + \sigma) & L - x \leq (2^{1/6} - 1)\sigma \\ 0 & L - x > (2^{1/6} - 1)\sigma \end{cases}, \quad (10)$$

$$F_{w,y}^{\text{bottom}}(x) = 0 \quad \forall x. \quad (11)$$

Throughout the paper we will be calculating the flow velocity, $\langle v_y \rangle$, which is the average of v_y over all \mathbf{v} and θ at a given \mathbf{r} . Anticipating this, we define the average particle velocity “at the wall,” v_w , to be the average velocity at $x \approx 0.35\sigma$, i.e.,

slightly outside the range of the wall potential. Note that in general $v_w \neq W$.

Finally, the overall density is specified by the particle area fraction $\phi \equiv N\pi\sigma^2/(4AL^2)$, where N is the number of particles and L and \mathcal{A} are defined as in Fig. 1.

C. Simulation parameters

Since we are interested in a range of values for the friction ξ , and particularly the large friction limit, we use the Brownian dynamics algorithm due to van Gunsteren and Berendsen, which is not limited by the restriction $\Delta t\xi \ll 1$ [63]. We set $\Delta t = 0.00005\tau$ and for a given L and ϕ adjust the aspect ratio \mathcal{A} (Fig. 1) to give 10^4 particles.

In general, the model considered here exhibits phase-separated states for sufficiently large ϕ and ℓ (see Refs. [24,26,64] for the phase diagram in the overdamped limit, noting that the Péclet number Pe is equal to $3\ell/\sigma$). In our case, however, we restrict attention to those values of ϕ and ℓ for which the bulk system is in a homogeneous fluid phase. Specifically, all simulations have $\phi \leq 0.5$ and $Pe \leq 30$, and the few simulations with $Pe = 30$ have $\phi \leq 0.3$. Since the presence of inertia only shifts the phase separation boundary towards higher ϕ and ℓ [65], it is sufficient to compare our values of ϕ and ℓ with the phase diagram in the overdamped limit.

To rule out finite-size effects, we choose L such that the channel dimensions are larger than any microscopic correlation length. Since we consider only values of ℓ and ϕ below the onset of critical behavior and phase separation, the only correlation lengths to consider are those of a single-particle trajectory in the absence of interactions, namely, ℓ and $\sqrt{D/\xi}$. The former is the active persistence length, while the latter is the distance a particle with characteristic velocity $\sqrt{D\xi}$ travels in a frictional time $1/\xi$. Depending on the value of the friction, L in the range 25σ – 100σ is large enough to rule out finite-size effects due to these lengths (see Appendix A for details). We begin recording statistics at $t = 200\tau$, when all trajectories reach steady state, and continue until $t = 1000\tau$.

III. RESULTS

In passive fluids described by the Boltzmann equation, the interaction timescales are the smallest in the model and therefore the primary mechanism behind thermalization and relaxation into local equilibrium. In the case of a passive fluid interacting with a substrate, however, there exists an additional timescale, the frictional time $1/\xi$, which can be comparable to or smaller than the mean-free time between collisions. Moreover, even in the absence of interparticle interactions, all momentum is dissipated into the substrate via the frictional mechanism. In these circumstances, momentum transport and dissipation are predominantly determined by the frictional and diffusive relaxation mechanisms, with interparticle interactions playing a supplementary role. Further, in the case of an active fluid, there exists the reorientation time $1/D_r$. This timescale influences how far the momentum from the wall penetrates into the bulk before being dissipated to the substrate. In the limit where the frictional and reorientation times are shorter than the mean-free time, the phenomenology

is most clearly understood by considering a system of non-interacting particles. Then the noninteracting case can be used as a baseline to interpret the phenomenology when the interactions modify it. This is the route we follow below.

Since we are interested in momentum transport, we focus on the flow velocity profiles $\langle v_y \rangle$. The corresponding density profiles have been well studied in limiting cases of our model [56,66–69]. Most notably, in the overdamped limit and in the absence of driving, particle accumulation is observed at the wall. On the other hand, density profiles in underdamped and driven systems have not been studied in depth. Our present simulations indicate nontrivial and potentially interesting behavior in this case, including depletion near the wall for small friction and zero activity. A few of these plots are shown in Appendix A; however, this subject deserves further study.

A. Dilute limit

In the dilute limit, the steady-state flow velocity $\langle v_y \rangle$ decays rapidly away from the boundary over a length scale determined by ξ and ℓ . This trend reflects the fact that, by virtue of their persistent motion, particles travel a short distance into the bulk before their momentum acquired at the boundary dissipates into the substrate.

A precise quantitative analysis could in principle be obtained using the Fokker-Planck equation associated with Eqs. (5)–(7), whose steady-state solution $f(\mathbf{r}, \theta, \mathbf{v})$ gives the probability of finding a particle with coordinates $(\mathbf{r}, \theta, \mathbf{v})$. The flow velocity profile could then be obtained as an average of v_y with respect to f . On general grounds, it is plausible that this analysis would yield a boundary layer consisting of a sum of exponentials (see, e.g., Ref. [56] for an explicit verification of this claim in the context of a simpler model). That is, the velocity profile would take the form

$$\langle v_y \rangle \sim \sum_k e^{-x/\lambda_k}, \quad (12)$$

where the λ_k could be obtained from a spectral analysis of the relevant Fokker-Planck operator.

In practice, this approach is difficult, and we do not attempt it for the current problem. On the other hand, it is not difficult to estimate the dimensional dependence of the leading order exponential, modulo two dimensionless constants estimated from simulations. Toward this end, we define a to be the decay length of the leading order exponential, so that

$$\langle v_y \rangle \approx e^{-x/a}. \quad (13)$$

We note that asymptotic single-exponential behavior has been obtained in steady-state density profiles in active systems [66,67,70–73]. Consistent with our analysis, Elgeti and Gompper [67] have also suggested that the true density profile (not just the asymptotic form) is a sum of exponentials.

For passive particles, the only microscopic length is $\sqrt{D/\xi}$, and so we take $a(\xi, \ell = 0) = c\sqrt{D/\xi}$ where c is a constant. Physically, the length $\sqrt{D/\xi}$ approximates the distance a passive particle with characteristic velocity $\sqrt{D\xi}$ travels in a frictional time $1/\xi$: this is how far a particle penetrates into the bulk before losing its momentum to the substrate.

In general, dimensional analysis implies that $a = c(v_c/\xi)$, where v_c is an appropriate characteristic velocity. For passive

particles, we already obtained $v_c = \sqrt{D\xi}$. For active particles, however, there is not only the thermal velocity $\sqrt{D\xi}$ which contributes to v_c , but also a characteristic active velocity $v_a = \ell t_a^{-1}$, where t_a is a characteristic time. For instance, if we assume that $\xi \gtrsim D_r = O(1)$; i.e., frictional relaxation is faster than orientational relaxation, then the relevant timescale is $1/\xi$, and v_a can be estimated as $F_p/(m\xi) = D_r\ell$. In the opposite limit, where orientational relaxation dominates, we have $v_a \sim F_p/(mD_r) = \xi\ell$.

Still, it is not obvious how these two velocities combine to give the appropriate v_c . Here we make a simple ansatz in the form of a root-mean-square combination, which leads to

$$a(\xi, \ell) = (c/\xi)\sqrt{D\xi + \mu v_a^2} \quad (14)$$

$$= \frac{c\sigma}{\xi_0^{1/2}} \sqrt{1 + \frac{\mu(\tau t_a^{-1})^2}{\xi_0} \left(\frac{\ell}{\sigma}\right)^2}, \quad (15)$$

where μ is a fitting parameter. We test this prediction in the case $\xi_0 = 1$ by performing an exponential fit on the asymptotic $\langle v_y \rangle$ profiles obtained from our simulations with noninteracting ABPs. The parameters resulting from the fit are $c = 0.9$ and $\mu(\tau t_a^{-1})^2 = 1.14$. As shown in Fig. 2, the results match the predicted scaling well. Further details on the fitting procedure are given in Appendix A.

B. Role of interactions

The discussion in the previous section applies in the dilute limit. We now examine how interactions modulate the behavior of the noninteracting system. For small to moderate friction ($\xi \lesssim 5$) we find qualitatively similar flow velocity profiles, with interactions either aiding or hindering momentum transport depending on the values of ξ and ℓ . For instance, Fig. 3 shows the flow velocity profiles for friction parameter $\xi = 0.1\tau^{-1}$ and several packing fractions for passive particles (Fig. 3 top) or active particles (Fig. 3 bottom). While increasing density increases momentum transport of passive particles, we observe the opposite effect for the active case. For large friction, there are more dramatic departures from the dilute limit within a few particle diameters from the wall. However, we postpone discussion of this phenomenon until the next section.

In a passive dilute gas, elementary mean-free-path theories provide a qualitatively accurate picture of macroscopic transport of momentum [74]. Here, also, we have been able to construct a mean-free-path theory which adequately explains the behavior of interacting systems with small to moderate friction. This theory is presented in Appendix B. The basic ideas underlying this kinetic theory can be explained by comparison of the respective length scales over which momentum is transported due to (A) thermal motion and (B) free active motion. In the absence of interactions, the first length scale corresponds to free Brownian motion: independent of active driving, particles travel a distance $\sim\sqrt{D/\xi}$ before their initial y momentum is dissipated into the substrate. The second length scale is determined by a characteristic active velocity v_a , which (again in the absence of interactions) causes particles to travel an average distance of v_a/ξ before losing their initial y momentum.

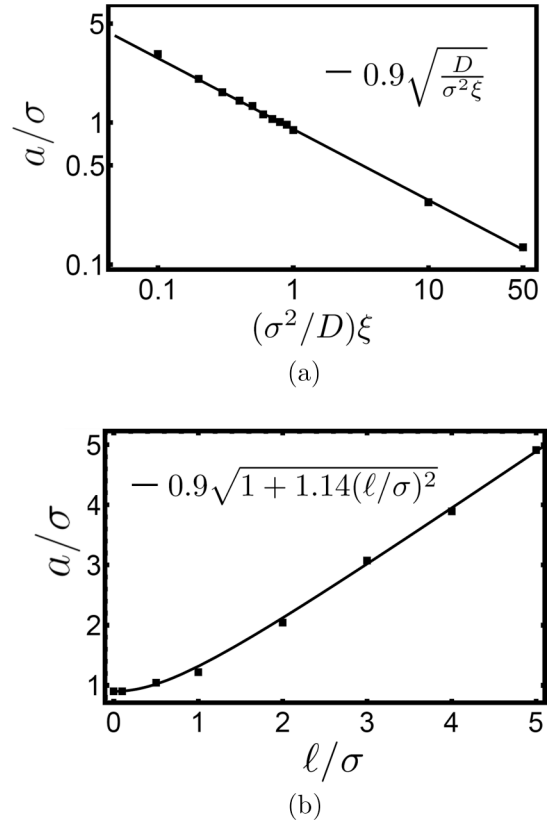


FIG. 2. Tests of the predictions in Sec. III A for the dependence of the momentum transfer length scale a on friction and activity. The value of a at each parameter set is obtained by fitting the flow velocity profiles of noninteracting systems to the form $\langle v_y \rangle = e^{-x/a}$. (a) a as a function of the nondimensional friction parameter ξ in passive systems ($\ell = 0$). (b) a as a function of active persistence length ℓ for fixed friction parameter $\xi = \tau^{-1}$. When fitting the value of a , we have excluded a boundary layer that exhibits deviations from exponential decay (see Appendix A and Fig. 9).

Interparticle interactions affect transport over these two length scales differently. Note first that interactions do not interrupt transport over length scale (A), since linear momentum is conserved during the (nearly instantaneous) collisions. In fact, interactions slightly aid transport in this case since collisions also involve instantaneous and lossless transport of momentum over a particle diameter. On the other hand, particle *orientation* is not transferred in collisions; i.e., a particle which would otherwise carry its y momentum over a length v_a/ξ might transfer its momentum to a particle oriented in the opposite direction, breaking transport across this length. Thus, interactions interfere with transport over length scale (B).

In light of these conclusions, it is reasonable to expect that in cases where length scale (A) dominates (B), interactions aid momentum transport; whereas when (B) dominates (A), the opposite is observed. The boundary between the two behaviors occurs when the length scales (A) and (B) are comparable: $v_a/\xi \sim \sqrt{D/\xi}$, or $v_a = C\sqrt{D\xi}$ where C is a constant. In fact, the more detailed kinetic theory in Appendix B arrives at the same prediction.

In Sec. III A we estimated $v_a \sim F_p/(m\xi) = D_r\ell$ in the limit $\xi \gg D_r$, and $v_a \sim F_p/(mD_r) = \xi\ell$ in the opposite limit. Using

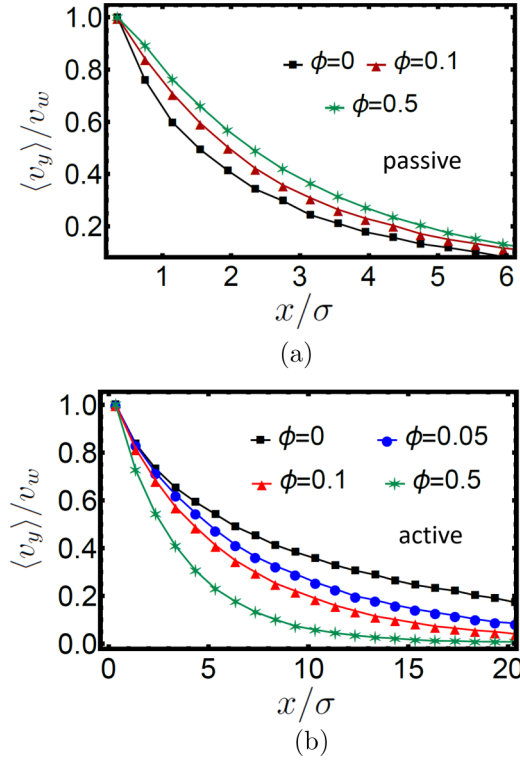


FIG. 3. Illustration of the effect of interparticle interactions on momentum transport. The flow velocity $\langle v_y \rangle$ is shown as a function of distance x from the boundary. For passive particles [$\ell = 0$, panel (a)], increasing the packing fraction ϕ increases momentum transport, whereas with sufficiently high activity [$\ell = 5\sigma$, panel (b)], the opposite is observed. In both cases $\xi = 0.1\tau^{-1}$.

these estimates, we can make the following predictions for the boundary in the (ℓ_0, ξ_0) space:

$$\ell_0 = a_1 \xi_0^{1/2}, \quad \xi_0 \gtrsim 1 \quad (16)$$

and

$$\ell_0 = a_2 \xi_0^{-1/2}, \quad \xi_0 \lesssim 1, \quad (17)$$

where $a_1 = 1.96$ and $a_2 = 0.28$ are constants obtained by fitting the expressions to a phase diagram in the (ℓ_0, ξ_0) space. The phase diagram is shown in Fig. 4, together with the fits [Eq. (16), solid line; Eq. (17), dashed line]. Red squares denote systems where interactions hinder transport, green circles where interactions aid transport, and yellow stars where the result is indeterminate. We classify each simulation to one of these categories by comparing the penetration depth of the flow velocity profile (cf. Fig. 3) at $\phi = 0, 0.05, 0.1, 0.2$ (Appendix A). We obtained the prefactors in Eqs. (16) and (17) by performing a best fit on the yellow (indeterminate) data points in the ranges $0.5 \leq \xi_0 \leq 5$ and $0.02 \leq \xi_0 \leq 0.2$.

C. Structure and transport at the wall

The system exhibits further nontrivial behavior *at* the wall (i.e., within roughly a particle diameter of the wall). Understanding the behavior in this region will be important for establishing proper boundary conditions on any continuum theory describing the bulk.

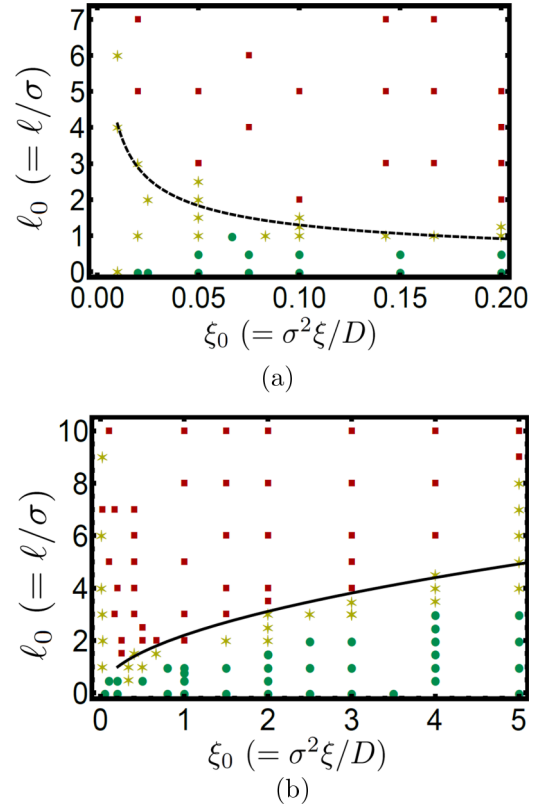


FIG. 4. Generalization of Fig. 3 to the entire (ξ_0, ℓ_0) space. The top and bottom panels, respectively, show the low- and high-friction regimes. Using the criterion discussed in the main text, red squares indicate parameter values for which interactions hinder transport, and green circles show values for which interactions aid transport. Yellow stars indicate cases where the effect of interactions could not be identified unambiguously (see Appendix A). The solid and dashed curves are estimates for the boundary between the two regimes, based on the kinetic picture discussed in Sec. III B.

1. Flow reversal

First, we observe *flow reversal* near the boundary for large friction and moderate activity. For instance, Fig. 5 shows the flow velocity profiles for $\xi = 30\tau^{-1}$, $\ell = 5\sigma$, and several packing fractions. In this case flow reversal occurs for the intermediate packing fraction: $\phi \approx 0.1$.

This flow reversal phenomenon is reminiscent of other behaviors in active systems that would be thermodynamically forbidden at equilibrium, such as spontaneous flow [37,39,40] and orientational order in the absence of torques [56,70]. The operating principle underlying these phenomena is the ability of conservative fields and geometric confinement to kinetically “sort” particles from an isotropic state into an orientationally ordered one. A similar mechanism drives flow reversal here, with interparticle interactions playing the role of the “sorting” force. More precisely, an active system initialized with the y component of the polarization P_y equal to 0 (the steady state in the absence of activity) evolves towards a state with $P_y \neq 0$.

The mechanism is illustrated in Fig. 6. We divide particles near the wall into two layers at distances $\approx \sigma$ and 2σ from the wall. We consider friction sufficiently large that the outer layer

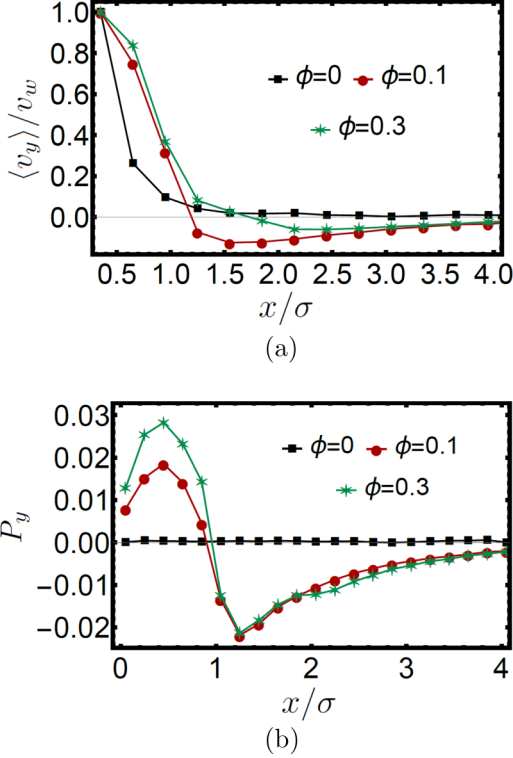


FIG. 5. An instance of flow reversal. Panel (a) shows the flow velocity as a function of distance from the wall x , and panel (b) shows the y component of the polarization. The corresponding density profiles are shown in Appendix A. The “kinetic sorting” mechanism illustrated in Fig. 6 induces this polarization, which itself generates the negative flow velocity seen in the top plot. The sorting mechanism depends on interparticle interactions and is optimized for intermediate values of the packing fraction ϕ . The uncertainty on each data point is negligible compared to the symbol size. Other parameter values are $\xi = 30\tau^{-1}$, $\ell = 5\sigma$, and $W = 5(D/\sigma)$.

has a much smaller flow velocity than the inner layer. Let us now consider two types of particles in the inner layer: type A oriented parallel to the direction of driving ($+y$ direction, $0 < \theta < \pi$) and type B antiparallel ($-y$ direction, $-\pi < \theta < 0$). Since flow reversal is observed only for large friction, we can

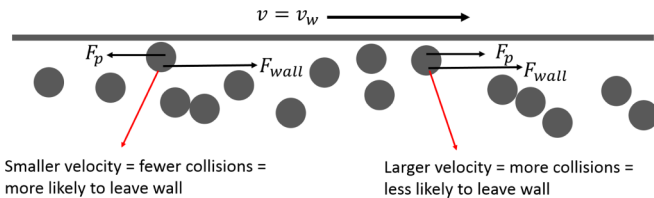


FIG. 6. An illustration of the discussed kinetic sorting mechanism. Particles are split into two types: those with orientation parallel to the driving (type A) and those with orientation opposite the driving (type B). Compared with their type B counterparts, type A particles on average undergo more collisions with particles in the secondary layer (at $\sim 2\sigma$ from the wall). Since these collisions tend to push particles back towards the wall, the system sorts into a polarized steady state where there are more type A particles at distance σ and more type B particles at distance 2σ .

write $v_a \sim D_r \ell$ (see Sec. III A), which leads to

$$|\langle v_y \rangle_A| - |\langle v_y \rangle_B| \approx |v_w + \alpha D_r \ell| - |v_w - \beta D_r \ell|, \quad (18)$$

where $0 \leq \alpha, \beta \leq 1$ are constants.

The variation of $|\langle v_y \rangle_A| - |\langle v_y \rangle_B|$ with ℓ can be made clearer by rewriting the absolute values:

$$|\langle v_y \rangle_A| - |\langle v_y \rangle_B| = \begin{cases} (\alpha + \beta)D_r \ell & \beta D_r \ell < v_w \\ 2v_w + (\alpha - \beta)D_r \ell & \beta D_r \ell \geq v_w \end{cases}. \quad (19)$$

For $0 < \beta D_r \ell < v_w$, $|\langle v_y \rangle_A| - |\langle v_y \rangle_B|$ is positive, increasing linearly with ℓ starting from 0. In the range $\beta D_r \ell \geq v_w$, it either increases or decreases with ℓ depending on the sign of $\alpha - \beta$. Clearly $\alpha = \beta$ in the absence of driving, since in this case the distribution of orientations is symmetric about the x axis. With driving, the symmetry is broken; however, since the general dynamics is torque-free and the orientational order induced by kinetic sorting is observed to be relatively small (see Fig. 5), we assume $\alpha \approx \beta$. If this is true, then we expect $|\langle v_y \rangle_A| - |\langle v_y \rangle_B|$ to be positive over a large range of ℓ . In what follows we therefore assume the positivity of $|\langle v_y \rangle_A| - |\langle v_y \rangle_B|$.

Now, the crux of the argument is this: since particles of type A on average possess velocities larger in magnitude than those of type B , they undergo more off-center collisions with particles in the outer layer. Since these types of collisions tend to push particles back towards the wall, type B particles can more easily escape the inner layer. In other words, if $r_X^{I \rightarrow O}$ is the rate of particle species X traveling from the inner to outer layer, then $r_B^{I \rightarrow O} > r_A^{I \rightarrow O}$. On the other hand, this asymmetry is not as pronounced for particles traveling from the outer layer to the inner one: $r_B^{O \rightarrow I} \approx r_A^{O \rightarrow I}$ (since the difference between A and B velocities is smaller in the outer layer). The overall imbalance of rates implies that the $P_y = 0$ state is not stable. We verify this prediction with simulation results, observing $P_y > 0$ in the inner layer and $P_y < 0$ in the outer layer (Fig. 5). Finally, orientational order can be connected to the flow velocity if $\xi \gg D_r$ and $\ell > \sqrt{D_r/\xi}$; i.e., active driving dominates thermal driving. In this case \mathbf{v} is approximately parallel to $\hat{\mathbf{u}}$, and therefore $P_y < 0$ corresponds to a negative contribution to the overall flow velocity.

In fact, it is possible to make a more precise prediction. Since $|\langle v_y \rangle_A| - |\langle v_y \rangle_B|$ increases monotonically with v_w until $D_r \ell \sim v_w$, we expect the induced polarization to also increase with v_w until $D_r \ell \sim v_w$. This trend is confirmed in Fig. 7. On the other hand, further increasing v_w results in a smaller polarization, despite the fact that $|\langle v_y \rangle_A| - |\langle v_y \rangle_B|$ saturates. This suggests that for large driving, particles of both types A and B collide so frequently that the asymmetry between the two is washed out; i.e., the difference in rates $r_B^{I \rightarrow O} - r_A^{I \rightarrow O}$ is no longer proportional to $|\langle v_y \rangle_A| - |\langle v_y \rangle_B|$.

2. Shear stress at the boundary

From an experimental standpoint, an important observable is the shear stress at the wall, σ_w , defined as the y component of the average force, per unit length, which particles exert on the wall. Note that since the wall potential [Eq. (4)] has finite width in our simulations, our measurement of wall stress includes all particles with $x/\sigma < 2^{1/6} - 1 \approx 0.123$.

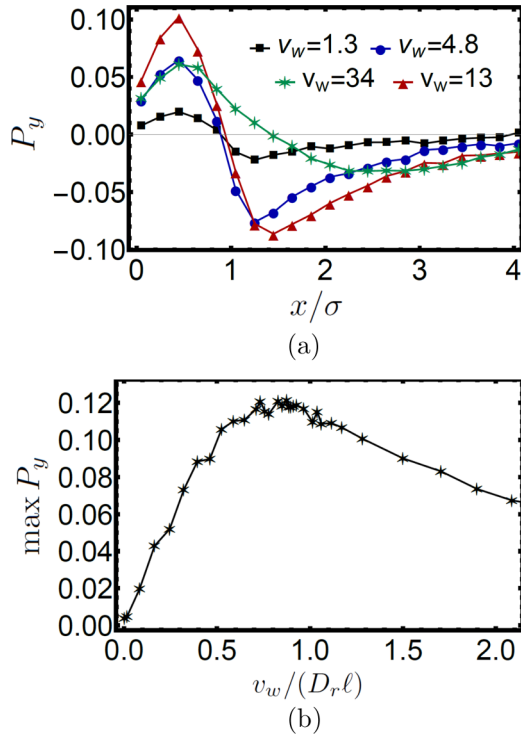


FIG. 7. Dependence of the flow reversal phenomenon on driving. (a) The y polarization for varying values of v_w (the particle velocity at the wall). In simulations v_w is indirectly varied by changing the parameter W in the wall force [Eq. (8)] over the range $W\tau^2/m\sigma \in [0.1, 200]$. (b) The *maximum* value of P_y for each v_w . The magnitude of the induced polarization is maximized when $D_r\ell \sim v_w$. Here $\xi = 30\tau^{-1}$, $\ell = 5\sigma$, and $\phi = 0.1$.

We observe that σ_w increases monotonically with activity (8). This result can be explained by the fact that more particles accumulate at the wall with higher activity, increasing the burden of shearing the system. However, we observe more complex behavior with varying density. First, we note that in a noninteracting system the stress increases linearly with

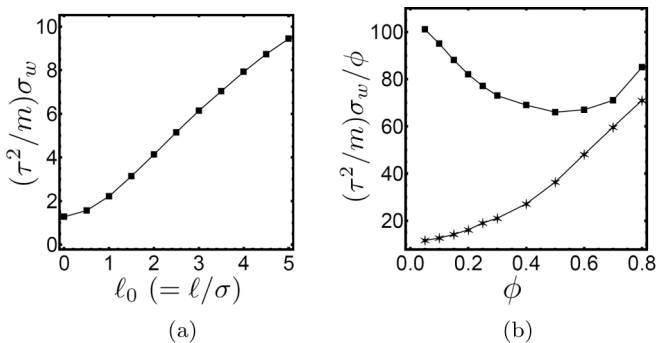


FIG. 8. (a) Stress at the wall σ_w as a function of ℓ for $\xi_0 = 10$ and $\phi = 0.1$. The stress increases monotonically, corresponding to increasing particle accumulation at the boundary. (b) σ_w as a function of packing fraction ϕ for $\xi_0 = 10$ and $l_0 = 5$ (squares) and $l_0 = 0$ (stars). To illustrate more clearly the effect of interactions, the y axis shows σ_w/ϕ : this is to factor out the linear dependence $\sigma_w \propto \phi$ already present in the noninteracting system.

packing fraction $v_w \sim \phi$. Thus we plot σ/ϕ (Fig. 8) to reveal effects due to interactions. For passive particles we find that the stress increases faster than ϕ , whereas for high activity the stress is sublinear in ϕ . To understand this observation, note that the y momentum dissipated into the substrate is proportional to the integral of the flow velocity, $\int \langle v_y(x) \rangle dx$. Since the wall is the dominant source of the average momentum, this implies that the stress at the wall is also proportional to $\int \langle v_y(x) \rangle dx$. Thus, if $v_y(x)$ penetrates farther into the bulk, stress at the wall is increased. On the other hand, recall from Sec. III B that the penetration depth of $v_y(x)$ increases with ϕ for passive particles and decreases with ϕ for active particles. The combination of these two effects implies that the stress at the wall should increase faster than ϕ for passive particles, and the opposite for sufficiently active particles, consistent with our observations.

IV. DISCUSSION

Using Brownian dynamics simulations and kinetic arguments, we have investigated the phenomenology of a boundary-driven active gas in a sheared channel geometry. We find that the nontrivial parts of this phenomenology are confined to a boundary layer characterized by the microscopic length scales ℓ (the active persistence length), $\sqrt{D/\xi}$ (the thermal persistence length), and σ (the particle diameter). We do not observe spontaneous flow or density inhomogeneities in the bulk for parameters below the onset of motility-induced phase separation.

Within the boundary layer, the mechanisms of momentum transport are dictated by the complex interplay among interparticle interactions, active forces, and boundary driving. We find that the flow velocity profiles decay exponentially when the distance from the wall is sufficiently large compared with all of the three microscopic lengths: $\sqrt{D/\xi}$, ℓ , and σ . Close to the wall, we observe nonexponential velocity profiles and even flow reversal. In general, we find that interparticle interactions can either aid or hinder momentum transport depending on system parameters.

Although we have rationalized these findings in terms of a simple kinetic picture, it is an open question whether a more systematic theoretical description in terms of appropriate hydrodynamic variables and constitutive relations exists. Our results suggest difficulties in developing this type of description, however. The nontrivial phenomenology is confined to a boundary layer which cannot be mapped onto a generic bulk description in terms of a finite set of hydrodynamic variables and associated constitutive relations.

Besides addressing such general questions, an interesting topic for future work will be to study the effect of phase separation on the shear response. Boundary driving will nontrivially influence the glassy dynamics observed in high-density, weakly active particle fluids [75–77] and could potentially exhibit phenomenology similar to shear jamming [78,79] and discontinuous shear thickening [80,81] seen in passive athermal suspensions. Further, given the coupling in active systems between orientational order and flow, it would be interesting to study the effect of torques at the boundary. Finally, the phenomena observed here will generally depend on the full distribution function at the boundary, and in

particular on the exact form of the driving force. However, our simulations show that the results from Sec. III are at least qualitatively robust against variations of the wall force. To further test the generality of this conclusion, it would be interesting to perform the types of analyses we describe here on other externally driven active matter systems.

Our simulation code and data are associated and can be accessed on the Open Science Framework (OSF) at Ref. [82].

ACKNOWLEDGMENTS

We acknowledge support from the Brandeis Center for Bioinspired Soft Materials, an NSF MRSEC, DMR-1420382 (C.G.W., A.B., M.F.H.), NSF DMR-1149266 and BSF-2014279 (C.G.W. and A.B.), and DMR-1855914 (M.F.H.). Computational resources were provided by the NSF through XSEDE computing resources (MCB090163) and the Brandeis HPCC, which is partially supported by the Brandeis MRSEC.

APPENDIX A: ADDITIONAL SIMULATION DETAILS

1. Simulation parameters

As described in the main text, all simulations contain 10^4 particles. On the other hand, we adjust the channel dimensions according to the following rules:

$$\xi_0 < 0.1 \rightarrow L = 100\sigma, \quad (\text{A1})$$

$$0.1 \leq \xi_0 < 1 \rightarrow L = 75\sigma, \quad (\text{A2})$$

$$1 \leq \xi_0 < 10 \rightarrow L = 50\sigma, \quad (\text{A3})$$

$$\xi_0 \geq 10 \rightarrow L = 25\sigma. \quad (\text{A4})$$

This enables improved statistics near the wall in simulations with large friction, where a large value of L is not required to exclude finite-size effects.

Obtaining sufficient statistics at some parameter sets requires additional simulations. To improve the quality of the fits in Fig. 2, at least 30 simulations are run in parallel at each data point and the results averaged. Moreover, for several data points in Fig. 4 with large friction and near the phase boundary, we average results over 15 independent simulations (in these cases the effect of density on the flow velocity profile is small and susceptible to noise). Finally, we obtain the results in Fig. 5 from averages over 100 independent simulations.

2. Dilute limit: Fits of $\langle v_y \rangle$

For each parameter set we fit $\langle v_y \rangle$ to the form $e^{-x/a}$. The fit is limited to the range $x/\ell_{\text{fit}} \in (1.5, 3.5)$, where $\ell_{\text{fit}} = \max(\sqrt{D/\xi}, \ell)$ approximates the distance over which a particle's motion is correlated in a system with no interactions or wall. We select the lower bound of this interval because nonexponential behavior is expected *a priori* for $x \lesssim \ell_{\text{fit}}$ [56] (the factor of 1.5 has been used for good measure). This expectation is confirmed by our simulation velocity profiles, which exhibit nonexponential behavior in this range; see Fig. 9 for several examples. The upper bound of the fit interval is set by the quality of our statistical sampling: as the velocity

profile $\langle v_y \rangle$ approaches 0, the quantity $\ln(\langle v_y \rangle/v_w)$ becomes noisy, which compromises the quality of the fit. Indeed, far enough from the wall, negative values of $\langle v_y \rangle$ are registered due to statistical noise; in these cases $\ln(\langle v_y \rangle/v_w)$ is not even defined. Choosing $3.5\ell_{\text{fit}}$ as the upper bound eliminates these statistical artifacts in all the fits.

3. Construction of the phase diagram

We construct the phase diagram in Fig. 4 using the following criteria. First, at each point in the (ξ_0, ℓ_0) space, we measure $\langle v_y \rangle$ for packing fractions $\phi = 0, 0.05, 0.1,$ and 0.2 . To quantify how far $\langle v_y \rangle$ penetrates into the bulk, we calculate for each value of ϕ the values of x for which $\langle v_y \rangle = 0.3v_w$ and $\langle v_y \rangle = 0.2v_w$, denoted as $x_{0.3}$ and $x_{0.2}$. Finally, we order these quantities with respect to ϕ . If $x_{0.3}$ and $x_{0.2}$ both increase monotonically with ϕ , we infer that interactions aid momentum transport, corresponding to green circles in Fig. 4. For the opposite trend, interactions hinder transport, corresponding to red squares. Any other ordering of $x_{0.3}$ and $x_{0.2}$ is assigned an indeterminate outcome denoted by yellow stars. The velocity profiles for one such point are shown in Fig. 10. A possible reason for an indeterminate outcome is random noise in the measured $\langle v_y \rangle$ due to the finite number of particle trajectories sampled in simulations. Alternately, the exact $\langle v_y \rangle$ might display nonmonotonic behavior near the wall due to interparticle interactions.

4. Density profiles

Representative density profiles are shown in Fig. 11.

APPENDIX B: KINETIC ARGUMENT FOR THE EFFECT OF INTERACTIONS

Recall from Sec. III B that increasing density increases momentum transport of passive particles but has the opposite effect for active particles. This phenomenon can be explained with a more careful consideration of the density dependence of the total momentum flux j_T , defined as the flux of the y component of momentum in the x direction. We write j_T as a sum of two contributions: a streaming contribution j_{stream} and a collisional contribution j_{coll} . The streaming piece is the momentum flux due to the streaming motion of the particles between collisions. The collisional piece is the same as was first considered by Enskog: at the instant of an interparticle collision, momentum is transferred across a length on the order of a particle diameter [74]. In the classical dilute gas, this mechanism results in a density-dependent increase to the viscosity.

If $f(\mathbf{r}, \theta, \mathbf{v})$ denotes the probability of finding a particle at position \mathbf{r} with orientation θ and velocity \mathbf{v} , then

$$j_{\text{stream}}(\mathbf{r}) = m \int dv_x dv_y d\theta f(\mathbf{r}, \theta, \mathbf{v}) v_x v_y. \quad (\text{B1})$$

This integral can be simplified on the hypothesis

$$\int dv_y d\theta f(\mathbf{r}, \theta, \mathbf{v}) v_y = 0, \quad \text{where } v_x < 0; \quad (\text{B2})$$

that is, the average y velocity of particles with negative x velocity is 0. This hypothesis is reasonable due to the dissipative

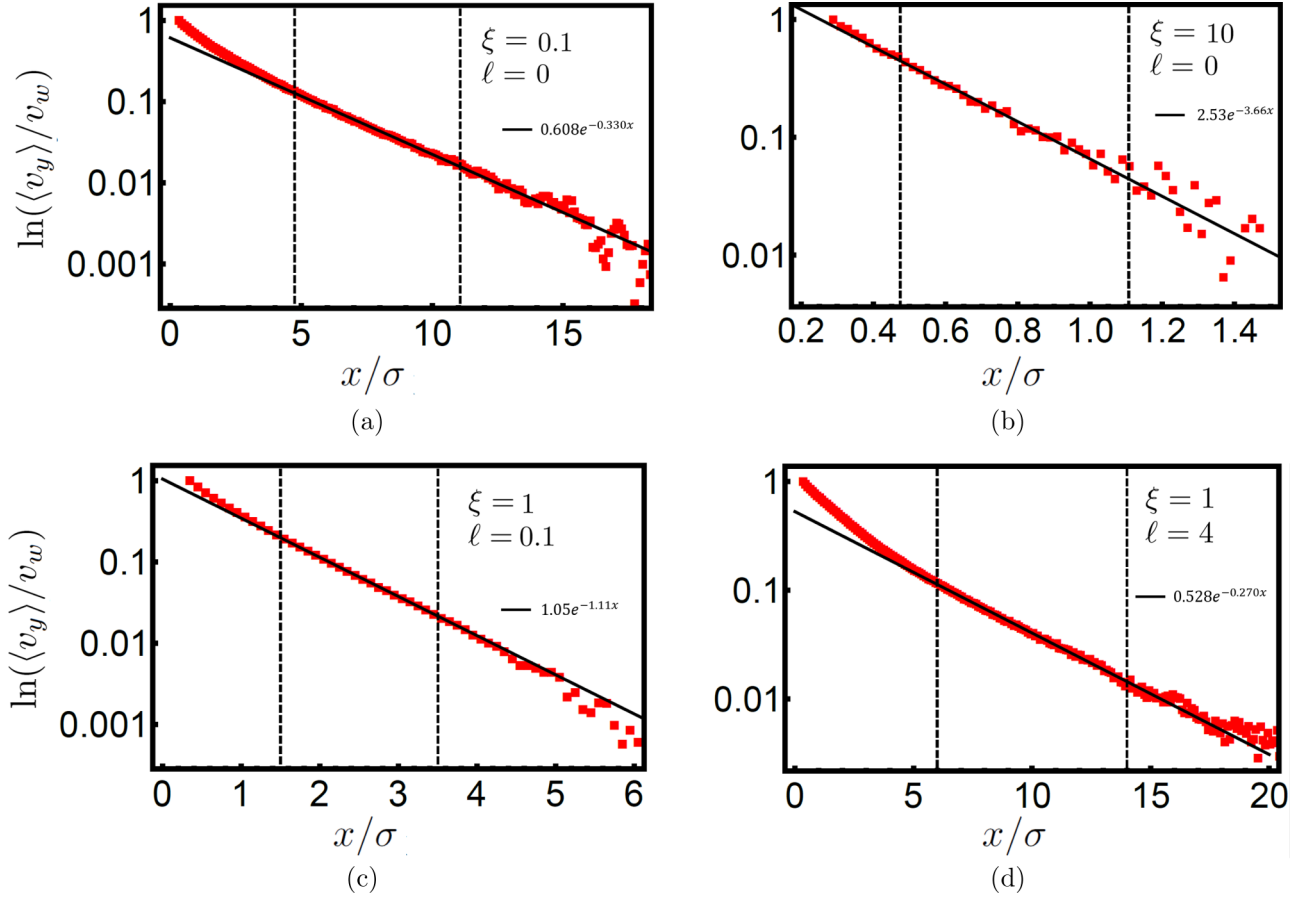


FIG. 9. Sample fits of the flow velocity profile $\langle v_y \rangle$ in the dilute limit. As explained in further detail in the text, the fit is performed over the range $x/\ell_{\text{fit}} \in (1.5, 3.5)$, where $\ell_{\text{fit}} = \max(\sqrt{D/\xi}, \ell)$. In the plots shown here, the fit range is enclosed by vertical dashed lines.

nature of the particle dynamics: consider a particle beginning with some $v_y, v_x > 0$ at $x = x_0$. Because of the persistence of particle trajectories, by the time a typical trajectory with such a starting point returns to $x = x_0$, one expects most of its initial y momentum to be lost to the substrate.

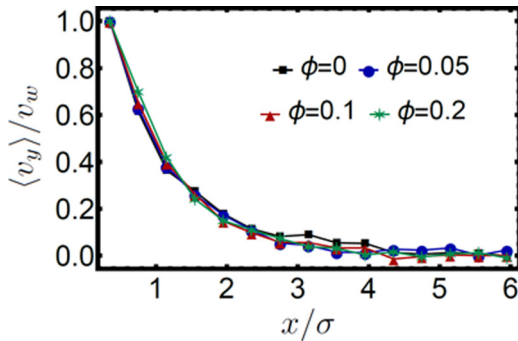


FIG. 10. Illustration of an “indeterminate” outcome in the phase diagram from Fig. 4. The flow velocity $\langle v_y \rangle$ is shown as a function of distance x from the boundary, for four different packing fractions. Simulation parameters are $\xi = 2\tau^{-1}$ and $\ell = 2\sigma$. The fact that the velocity profiles overlap prevents an unambiguous determination of the effect of interactions on momentum transport.

Under this hypothesis, Eq. (B1) becomes

$$j_{\text{stream}}(\mathbf{r}) = m \int_{v_x > 0} dv_x dv_y d\theta f(\mathbf{r}, \theta, \mathbf{v}) v_x v_y. \quad (\text{B3})$$

If we moreover assume that $f(\mathbf{r}, \theta, \mathbf{v}) = g(\mathbf{r}, v_x)h(\mathbf{r}, v_y)/2\pi$, i.e., the angles θ are distributed uniformly and v_x is independent of v_y wherever $v_x > 0$, then

$$j_{\text{stream}}(\mathbf{r}) = m \int_{v_x > 0} dv_x v_x g(\mathbf{r}, v_x) \int dv_y v_y h(\mathbf{r}, v_y) \quad (\text{B4})$$

$$= m\rho(\mathbf{r})\langle v_y \rangle \left[\frac{\int_{v_x > 0} dv_x v_x g(\mathbf{r}, v_x)}{\int dv_x g(\mathbf{r}, v_x)} \right] \quad (\text{B5})$$

$$\equiv m\rho(\mathbf{r})\langle v_y \rangle \cdot C_1 v_{\text{avg}}, \quad (\text{B6})$$

where C_1 is a constant and the last equation defines v_{avg} . The scalar velocity v_{avg} can be identified as a characteristic velocity related to the magnitude of the fluctuations of v_x about its mean. With this interpretation, it is reasonable to estimate this quantity in the dilute limit as proportional to the root-mean-square combination of the thermal velocity $\sqrt{D\xi}$ and a characteristic active velocity. For the latter quantity we previously used v_a , defined as the characteristic velocity due to free active motion in the absence of interparticle interactions (see Sec. III A).

On the other hand, at finite density, interparticle interactions tend to block the self-propelled motion of a particle,

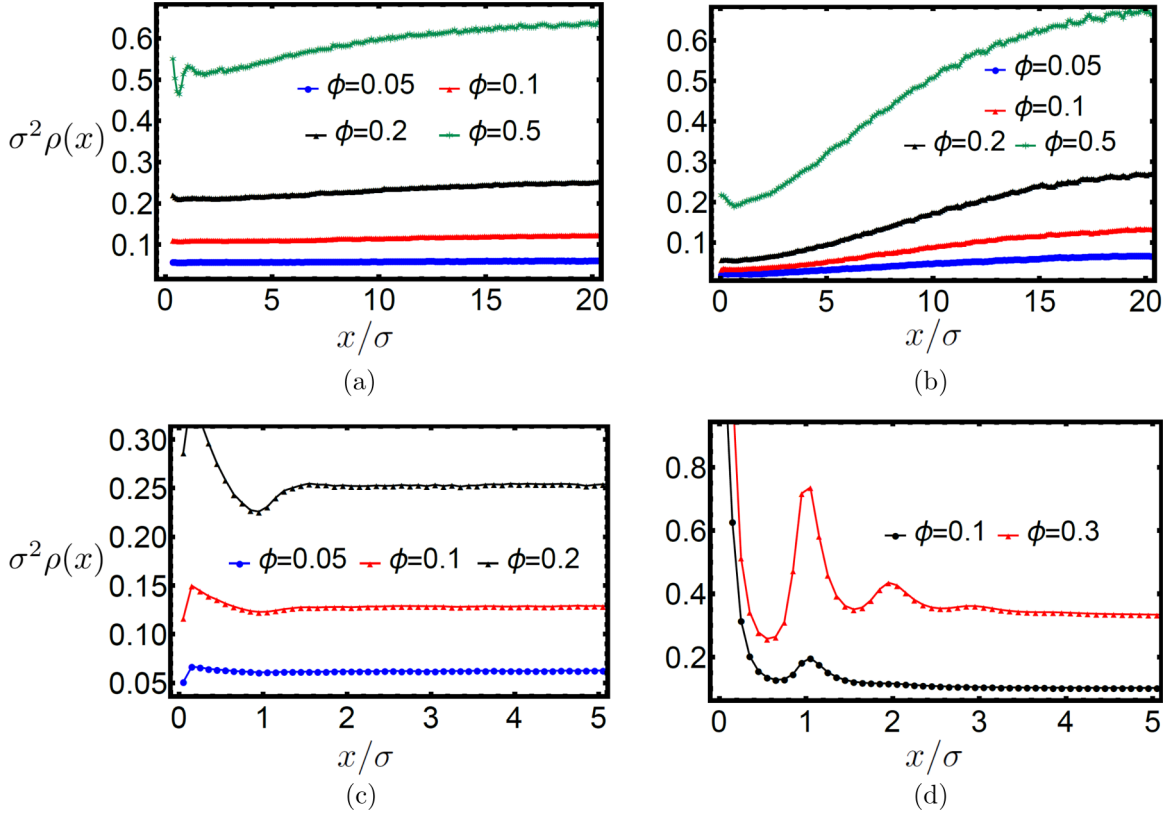


FIG. 11. Sample density profiles for $(\xi, \ell) = (0.1\tau^{-1}, 5\sigma)$ (top left); $(\xi, \ell) = (0.1\tau^{-1}, 0)$ (top right); $(\xi, \ell) = (5\tau^{-1}, 0)$ (bottom left); $(\xi, \ell) = (30\tau^{-1}, 5\sigma)$ (bottom right). The units on ρ are (particles/length²), and the normalization is that ρ integrated over the entire channel (both x and y coordinates) equals $N = 10000$, the total number of particles. Note that due to translational invariance, ρ is a function of x only. The top two figures correspond to Fig. 3, and the bottom right figure corresponds to the flow reversal phenomenon shown in Fig. 5.

which decreases the net momentum flux. More precisely, collisions tend to destroy the positive correlation between v_x and v_y which defines the momentum flux. For example, a particle moving in the positive x direction, with positive $\cos\theta$ and v_y , might collide with and transfer y momentum to a second particle whose self-propulsion points in the opposite direction, i.e., with $\cos\theta < 0$. In this case momentum transport into the bulk is interrupted in comparison with the case where no collision occurred. In general, because particle orientation is not transferred during a collision, collisions tend to destroy the correlation between $\cos\theta$ and v_y , and by extension between v_x and v_y . We model this decrease in momentum flux by introducing a density-dependent active velocity, denoted by $v_a^I[\rho(\mathbf{r})]$, a function of ρ . The analog to v_{avg} in this case is then denoted by $v_{\text{avg}}^I[\rho(\mathbf{r})]$:

$$v_{\text{avg}}^I[\rho(\mathbf{r})] = \sqrt{\{v_a^I[\rho(\mathbf{r})]\}^2 + D\xi}. \quad (\text{B7})$$

At low densities, we can expand to first order in ρ ,

$$v_{\text{avg}}^I[\rho(\mathbf{r})] = \sqrt{v_a^2[1 - C_3\sigma^2\rho(\mathbf{r}) + O(\rho(\mathbf{r})^2)]^2 + D\xi} \quad (\text{B8})$$

$$= v_0 - C_3\sigma^2 \frac{v_a^2}{v_0} \rho(\mathbf{r}) + O[\rho(\mathbf{r})^2], \quad (\text{B9})$$

where $C_3 > 0$ and $v_0 \equiv \sqrt{v_a^2 + D\xi}$.

An expression for j_{coll} can be obtained along similar lines to the above arguments, the only major difference being the

replacement of v_{avg} by $v_{\text{avg}} \cdot \pi\sigma^2\rho(\mathbf{r})$, which factors in the rate of collisions. Putting the pieces together, we have

$$j_T = j_{\text{stream}} + j_{\text{coll}} \quad (\text{B10})$$

$$\begin{aligned} &\approx C_1 v_{\text{avg}}^I(\rho(\mathbf{r})) \cdot \underbrace{m\rho(\mathbf{r})\langle v_y \rangle}_{\text{momentum density}} \\ &\quad \underbrace{j_{\text{stream}}} \\ &+ C_2 v_{\text{avg}} \cdot \pi\sigma^2\rho(\mathbf{r}) \cdot \underbrace{m\rho(\mathbf{r})\langle v_y \rangle}_{j_{\text{coll}}} + O[\rho(\mathbf{r})^3]. \end{aligned} \quad (\text{B11})$$

Substituting for v_{avg} and $v_{\text{avg}}^I(\rho(\mathbf{r}))$ gives

$$j_T = C_1 v_0 m\rho(\mathbf{r})\langle v_y \rangle \quad (\text{B12})$$

$$- C_1 C_3 \sigma^2 \frac{v_a^2}{v_0} m\rho(\mathbf{r})^2 \langle v_y \rangle \quad (\text{B13})$$

$$+ C_2 v_0 m\rho(\mathbf{r})^2 \pi\sigma^2 \langle v_y \rangle + O[\rho(\mathbf{r})^3]. \quad (\text{B14})$$

Except for dense systems, we expect the density $\rho(\mathbf{r})$ to be proportional to ϕ , that is,

$$\rho(\mathbf{r}) = \phi\Gamma(x), \quad (\text{B15})$$

where $\Gamma(x)$ is a positive function that depends on the location in the (ℓ, ξ) parameter space but is independent of ϕ .

In steady state, conservation of the y component of momentum gives

$$\frac{dj_T}{dx} = (\text{momentum source/sink}) \quad (\text{B16})$$

$$= -\xi m \rho(\mathbf{r}) \langle v_y \rangle \quad (\text{B17})$$

$$\approx -\xi m \phi \Gamma(x) \langle v_y \rangle. \quad (\text{B18})$$

Substituting j_T and absorbing numerical factors into the constants gives

$$\frac{d\langle v_y \rangle}{dx} = -\xi \left\{ C_1 v_0 \left[1 + \left(\frac{C_2}{C_1} - C_3 \frac{v_a^2}{v_0^2} \right) \sigma^2 \phi \Gamma(x) \right] \right\}^{-1} \langle v_y \rangle. \quad (\text{B19})$$

The resulting velocity profile is in general nonexponential, since $\Gamma(x)$ is not a constant. However, our simulations indicate that the deviation from a true exponential is not too dramatic; hence it is still reasonable to consider an (approximate) decay length. With this in mind, the decay length of the flow velocity

profile increases with ϕ if

$$\Lambda \equiv \frac{C_2}{C_1} - C_3 \frac{v_a^2}{v_a^2 + D\xi} > 0, \quad (\text{B20})$$

which is certainly true if $v_a = 0$, since C_1 and C_2 are positive. Without knowing the relative magnitudes of the constants, it is not possible to say whether Λ changes sign as v_a increases from 0. However, simulations indicate the change in sign does indeed occur; we therefore proceed on the hypothesis that a more detailed kinetic analysis would reach the same conclusion. Then the change in sign will occur when

$$\frac{C_2}{C_1} - C_3 \frac{v_a^2}{v_a^2 + D\xi} = 0 \quad (\text{B21})$$

$$\rightarrow v_a = C \sqrt{D\xi}, \quad (\text{B22})$$

where C is a new constant. This is the same criterion that was reached in Sec. III B [see the two paragraphs preceding Eqs. (16) and (17)].

-
- [1] S. Ramaswamy, *Annu. Rev. Condens. Matter Phys.* **1**, 323 (2010).
- [2] M. C. Marchetti, J. F. Joanny, S. Ramaswamy, T. B. Liverpool, J. Prost, M. Rao, and R. A. Simha, *Rev. Mod. Phys.* **85**, 1143 (2013).
- [3] J. Elgeti, R. Winkler, and G. Gompper, *Rep. Prog. Phys.* **78**, 056601 (2015).
- [4] C. Bechinger, R. Di Leonardo, H. Löwen, C. Reichhardt, G. Volpe, and G. Volpe, *Rev. Mod. Phys.* **88**, 045006 (2016).
- [5] A. Zottl and H. Stark, *J. Phys. Condens. Matter* **28**, 253001 (2016).
- [6] J. Elgeti and G. Gompper, *Eur. Phys. J. Spec. Top.* **225**, 2333 (2016).
- [7] N. Yoshinaga, *J. Phys. Soc. Jpn.* **86**, 101009 (2017).
- [8] D. Saintillan, *Annu. Rev. Fluid Mech.* **50**, 563 (2018).
- [9] U. Seifert, *Annu. Rev. Condens. Matter Phys.* **10**, 171 (2019).
- [10] D. Needleman and Z. Dogic, *Nat. Rev. Mater.* **2**, 17048 (2017).
- [11] V. Schaller, C. A. Weber, B. Hammerich, E. Frey, and A. R. Bausch, *Proc. Natl. Acad. Sci. USA* **108**, 19183 (2011).
- [12] T. Sanchez, D. T. N. Chen, S. J. DeCamp, M. Heymann, and Z. Dogic, *Nature (London)* **491**, 431 (2012).
- [13] C. Dombrowski, L. Cisneros, S. Chatkaew, R. E. Goldstein, and J. O. Kessler, *Phys. Rev. Lett.* **93**, 098103 (2004).
- [14] A. Kaiser, A. Peshkov, A. Sokolov, B. ten Hagen, H. Löwen, and I. S. Aranson, *Phys. Rev. Lett.* **112**, 158101 (2014).
- [15] J. Palacci, C. Cottin-Bizonne, C. Ybert, and L. Bocquet, *Phys. Rev. Lett.* **105**, 088304 (2010).
- [16] V. Narayan, N. Menon, and S. Ramaswamy, *J. Stat. Mech.* (2006) P01005.
- [17] V. Narayan, S. Ramaswamy, and N. Menon, *Science* **317**, 105 (2007).
- [18] A. Bricard, J.-B. Caussin, N. Desreumaux, O. Dauchot, and D. Bartolo, *Nature (London)* **503**, 95 (2013).
- [19] J. Deseigne, S. Leonard, O. Dauchot, and H. Chate, *Soft Matter* **8**, 5629 (2012).
- [20] G. Junot, G. Briand, R. Ledesma-Alonso, and O. Dauchot, *Phys. Rev. Lett.* **119**, 028002 (2017).
- [21] C. Becco, N. Vandewalle, J. Delcourt, and P. Poncin, *Physica A (Amsterdam)* **367**, 487 (2006).
- [22] D. S. Cambuí and A. Rosas, *Physica A (Amsterdam)* **391**, 3908 (2012).
- [23] A. Attanasi, A. Cavagna, L. Del Castello, I. Giardina, T. S. Grigera, A. Jelic, S. Melillo, L. Parisi, O. Pohl, E. Shen, and M. Viale, *Nat. Phys.* **10**, 691 (2014).
- [24] M. C. Marchetti, Y. Fily, S. Henkes, A. Patch, and D. Yllanes, *Curr. Opin. Colloid Interface Sci.* **21**, 34 (2016).
- [25] Y. Fily and M. C. Marchetti, *Phys. Rev. Lett.* **108**, 235702 (2012).
- [26] G. S. Redner, M. F. Hagan, and A. Baskaran, *Phys. Rev. Lett.* **110**, 055701 (2013).
- [27] G. S. Redner, A. Baskaran, and M. F. Hagan, *Phys. Rev. E* **88**, 012305 (2013).
- [28] J. Stenhammar, A. Tiribocchi, R. J. Allen, D. Marenduzzo, and M. E. Cates, *Phys. Rev. Lett.* **111**, 145702 (2013).
- [29] I. Buttinoni, J. Bialké, F. Kümmel, H. Löwen, C. Bechinger, and T. Speck, *Phys. Rev. Lett.* **110**, 238301 (2013).
- [30] B. M. Mognetti, A. Saric, S. Angioletti-Uberti, A. Cacciuto, C. Valeriani, and D. Frenkel, *Phys. Rev. Lett.* **111**, 245702 (2013).
- [31] J. Stenhammar, D. Marenduzzo, R. J. Allen, and M. E. Cates, *Soft Matter* **10**, 1489 (2014).
- [32] A. Wysocki, R. G. Winkler, and G. Gompper, *Europhys. Lett.* **105**, 48004 (2014).
- [33] M. E. Cates and J. Tailleur, *Annu. Rev. Condens. Matter Phys.* **6**, 219 (2015).
- [34] J. Stenhammar, R. Wittkowski, D. Marenduzzo, and M. E. Cates, *Phys. Rev. Lett.* **114**, 018301 (2015).
- [35] R. Ni, M. A. Cohen Stuart, M. Dijkstra, and P. G. Bolhuis, *Soft Matter* **10**, 6609 (2013).
- [36] G. S. Redner, C. G. Wagner, A. Baskaran, and M. F. Hagan, *Phys. Rev. Lett.* **117**, 148002 (2016).
- [37] J. Tailleur and M. E. Cates, *Europhys. Lett.* **86**, 60002 (2009).

- [38] M. B. Wan, C. J. Olson Reichhardt, Z. Nussinov, and C. Reichhardt, *Phys. Rev. Lett.* **101**, 018102 (2008).
- [39] L. Angelani, R. Di Leonardo, and G. Ruocco, *Phys. Rev. Lett.* **102**, 048104 (2009).
- [40] P. K. Ghosh, V. R. Misko, F. Marchesoni, and F. Nori, *Phys. Rev. Lett.* **110**, 268301 (2013).
- [41] B.-Q. Ai and F.-G. Li, *Soft Matter* **13**, 2536 (2017).
- [42] C. O. Reichhardt and C. Reichhardt, *Annu. Rev. Condens. Matter Phys.* **8**, 51 (2017).
- [43] J. Harder, S. A. Mallory, C. Tung, C. Valeriani, and A. Cacciuto, *J. Chem. Phys.* **141**, 194901 (2014).
- [44] R. Ni, M. A. Cohen Stuart, and P. G. Bolhuis, *Phys. Rev. Lett.* **114**, 018302 (2015).
- [45] L. Angelani, C. Maggi, M. L. Bernardini, A. Rizzo, and R. Di Leonardo, *Phys. Rev. Lett.* **107**, 138302 (2011).
- [46] Y. Baek, A. P. Solon, X. Xu, N. Nikola, and Y. Kafri, *Phys. Rev. Lett.* **120**, 058002 (2018).
- [47] J. Rodenburg, S. Paliwal, M. de Jager, P. G. Bolhuis, M. Dijkstra, and R. van Roij, *J. Chem. Phys.* **149**, 174910 (2018).
- [48] L. Caprini, U. M. B. Marconi, and A. Vulpiani, *J. Stat. Mech.* (2018) 033203.
- [49] M. Wang and A. Y. Grosberg, *J. Stat. Phys.* **175**, 640 (2019).
- [50] K. Klymko, D. Mandal, and K. K. Mandadapu, *J. Chem. Phys.* **147**, 194109 (2017).
- [51] J. M. Epstein, K. Klymko, and K. K. Mandadapu, *J. Chem. Phys.* **150**, 164111 (2019).
- [52] S. Steffenoni, G. Falasco, and K. Kroy, *Phys. Rev. E* **95**, 052142 (2017).
- [53] T. GrandPre and D. T. Limmer, *Phys. Rev. E* **98**, 060601(R) (2018).
- [54] Y. Fily, A. Baskaran, and M. F. Hagan, *Phys. Rev. E* **91**, 012125 (2015).
- [55] A. P. Solon, Y. Fily, A. Baskaran, M. E. Cates, Y. Kafri, M. Kardar, and J. Tailleur, *Nat. Phys.* **11**, 673 (2015).
- [56] C. G. Wagner, M. F. Hagan, and A. Baskaran, *J. Stat. Mech.* (2017) 043203.
- [57] W. Yan and J. F. Brady, *Soft Matter* **14**, 279 (2018).
- [58] L. Walsh, C. G. Wagner, S. Schlossberg, C. Olson, A. Baskaran, and N. Menon, *Soft Matter* **13**, 8964 (2017).
- [59] S. Shankar and M. C. Marchetti, *Phys. Rev. E* **98**, 020604(R) (2018).
- [60] Y. Fily, Y. Kafri, A. P. Solon, J. Tailleur, and A. Turner, *J. Phys. A* **51**, 044003 (2017).
- [61] C. Scholz, S. Jahanshahi, A. Ldov, and H. Löwen, *Nat. Commun.* **9**, 5156 (2018).
- [62] J. D. Weeks, D. Chandler, and H. C. Andersen, *J. Chem. Phys.* **54**, 5237 (1971).
- [63] W. van Gunsteren and H. Berendsen, *Mol. Phys.* **45**, 637 (1982).
- [64] P. Digregorio, D. Levis, A. Suma, L. F. Cugliandolo, G. Gonnella, and I. Pagonabarraga, *Phys. Rev. Lett.* **121**, 098003 (2018).
- [65] C. Dai, I. Bruss, and S. Glotzer, "The bumper boats effect: Effect of inertia on self propelled active particles systems", paper presented at the 2017 APS March meeting, New Orleans, Louisiana (unpublished).
- [66] C. F. Lee, *New J. Phys.* **15**, 055007 (2013).
- [67] J. Elgeti and G. Gompper, *Europhys. Lett.* **101**, 48003 (2013).
- [68] B. Ezhilan, R. Alonso-Matilla, and D. Saintillan, *J. Fluid Mech.* **781**, R4 (2015).
- [69] L. Caprini and U. Marini Bettolo Marconi, *Soft Matter* **14**, 9044 (2018).
- [70] M. Enculescu and H. Stark, *Phys. Rev. Lett.* **107**, 058301 (2011).
- [71] W. Yan and J. F. Brady, *J. Fluid Mech.* **785**, R1 (2015).
- [72] J. Elgeti and G. Gompper, *Europhys. Lett.* **109**, 58003 (2015).
- [73] A. Duzgun and J. V. Selinger, *Phys. Rev. E* **97**, 032606 (2018).
- [74] S. Chapman and T. Cowling, *The Mathematical Theory of Non-uniform Gases*, 3rd ed. (Cambridge University Press, Cambridge, 1970).
- [75] L. Berthier, *Phys. Rev. Lett.* **112**, 220602 (2014).
- [76] E. Flenner, G. Szamel, and L. Berthier, *Soft Matter* **12**, 7136 (2016).
- [77] R. Mandal, P. J. Bhuyan, P. Chaudhuri, C. Dasgupta, and M. Rao, Extreme active matter at high densities (unpublished).
- [78] D. Bi, J. Zhang, B. Chakraborty, and R. P. Behringer, *Nature (London)* **480**, 355 (2011).
- [79] I. R. Peters, S. Majumdar, and H. M. Jaeger, *Nature (London)* **532**, 214 (2016).
- [80] A. Fall, F. Bertrand, D. Hautemayou, C. Mezière, P. Moucheront, A. Lemaître, and G. Ovarlez, *Phys. Rev. Lett.* **114**, 098301 (2015).
- [81] E. Brown and H. M. Jaeger, *Rep. Prog. Phys.* **77**, 046602 (2014).
- [82] C. Wagner, data for "Response of active Brownian particles to boundary driving", <https://doi.org/10.17605/OSF.IO/QFWYK> (2019).